Area-Selective Atomic/Molecular Layer Deposition of Photoluminescent Europium-Organic Thin Films for Graphene-Based Heterostructures

Aleksei V. Emelianov,[1] Kamila K. Mentel,[1] Amr Ghazy,[2] Yu-Han Wang,[1] Andreas Johansson,[1,3] Maarit Karppinen,[2,*] Mika Pettersson[1,*]

[1]*Nanoscience Center, Department of Chemistry University of Jyväskylä, FI-40014 Jyväskylä, Finland*

[2]*Department of Chemistry and Materials Science, School of Chemical Engineering, Aalto University, FI-00076 Aalto, Espoo, Finland*

[3]*Nanoscience Center, Department of Physics University of Jyväskylä, FI-40014 Jyväskylä, Finland*

*e-mail: maarit.karppinen@aalto.fi

*e-mail: mika.j.pettersson@jyu.fi

Abstract

Developing area-selective atomic and molecular layer deposition (ALD/MLD) on 2D structures is crucial for optoelectronic and sensor applications yet remains challenging due to surface inertness. Here, we investigated the area-selective ALD/MLD of luminescent lanthanide-organic materials on graphene. To overcome the inherent chemical inertness of 2D materials, we utilized direct femtosecond laser two-photon oxidation to activate predefined regions on single-layer graphene, enabling area-selective deposition of europium-organic thin films. By optimizing the deposition parameters and carefully choosing a transfer polymer, we achieved over 90% selectivity and high film homogeneity in the activated areas. When excited with a green laser, the resulting films exhibited high photoluminescence emission at 612 nm and weaker emission bands at 579, 592, and 652 nm. In addition, graphene/Eu-organic thin films demonstrated green emission at ≈566 nm. The presence of graphene also shortened the photoluminescence lifetime due to quenching. Moreover, the Eu-organic layer reduced the work function of the oxidized graphene, indicating a strong electronic interaction in the graphene/Eu-organic heterostructures. This method enables the precise patterning of complex structures with submicron resolution, with potential for integration into multifunctional graphene-based optoelectronic and sensor systems on a single chip.

Keywords: graphene, femtosecond laser, area-selective deposition, ALD/MLD, luminescence

Introduction

Graphene heterostructures and 3D architectures, intricately patterned and combined with various functional materials, exhibit diverse properties and hold significant potential for advancing opto- and bioelectronics, sensors, and energy conversion and storage technologies.[1] Current patterning techniques mainly employ wet chemistry, focus on 2D functionalities, and do not allow vertical stacking in desired places.[2] Atomic layer deposition (ALD) and molecular layer deposition (MLD) are useful tools to control thin film growth on different surfaces.[3] Both methods provide uniform layer-by-layer growth over large areas, while MLD uses organic precursors instead of inorganic or metal-based reactants.[4] The modularity of these techniques enables their combination into a process known as atomic/molecular layer deposition (ALD/MLD). This combined approach has been shown to produce metal-organic thin films with enhanced mechanical and optoelectronic properties.[3b,5]

Area-selective deposition (ASD) is increasingly being explored as a promising alternative to conventional top-down methods,[6] offering the advantage of reducing edge placement errors.[7] ASD enables thin film growth predominantly on designated surfaces,[8] even when multiple different surfaces are present under identical processing conditions.[9] To maximize the effectiveness of ASD, it is crucial to differentiate between growth areas (GA) and non-growth areas (NGA) by using bottom-up process technology to achieve high selectivity.[10]

Area-selective ALD (AS-ALD) and MLD (AS-MLD) have already been employed on many materials,[11] including the growth of 2D materials (2DM).[12] Utilizing inhibitors to suppress the deposition in undesired areas is the dominant method in current ASD,[13] however, it requires additional lithographic steps.[14] Due to the inherent 2D nature, the surface of 2DM does not provide sufficient reactive sites for the chemisorption of ALD/MLD precursors compared with traditional microelectronics.[15] While AS-ALD has been demonstrated on 2DM,[16] its combination with AS-MLD remains largely unexplored. Functionalization of distinct surface areas is required to allow the selective growth of materials. Selectivity can be enhanced using surface functionalization by self-assembled monolayers,[17] electron beam irradiation,[18] UV exposure,[19] oxygen plasma treatment,[20] or by growing lateral superlattices.[21]

Recently, we proposed a way to overcome the chemical inertness of graphene to ALD precursors by locally activating the surface using direct femtosecond laser (fs-laser) two-photon oxidation (TPO) for area-selective ZnO deposition.[22] This method photochemically attaches oxygen-containing groups to graphene by exposing it to ultrafast laser pulses under an ambient atmosphere.[23] As a result, hydroxyl and epoxy groups form on the graphene surface with moderate laser exposure, while carbonyl and carboxyl groups appear at higher irradiation doses, closer to the ablation threshold.[24] TPO provides precise control over the oxidation level of graphene and enables the patterning of complex structures with high spatial resolution (~300 nm), with the potential to achieve 20 nm resolution using tip-enhanced techniques.[25] Additionally, this is a simple, resist-free ultrafast direct laser writing (UDLW) method,[26] and the oxidized graphene surface can be restored to its initial state through thermal annealing in an inert atmosphere.[22]

Here, we report the first AS-ALD/MLD for metal-organic thin films on graphene. Europium-organic thin films deposited via ALD/MLD show interesting photoluminescence properties, which are difficult to achieve using typical ALD of europium-oxide.[27] We combined UDLW and ASD to develop luminescent graphene/Eu-organic heterostructures in predefined areas using TPO. We achieved high homogeneity and over 90% selectivity in locally activated graphene regions for Eu-organic films up to 11 nm. The fabricated graphene/Eu-organic thin films exhibited high photoluminescence emission even when excited with a continuous wave (CW) 532 nm laser, while Eu^{3+} ions typically require UV excitation. These ALD/MLD films can also act as inhibitors for subsequent depositions,[28] allowing for the addition of new functionalities to graphene-based heterostructure devices.

Results and Discussion

Area-Selective ALD/MLD on Graphene

The process of area-selective ALD/MLD growth of Europium-1,4-benzene dicarboxylate (Eu-BDC) on graphene is illustrated in **Figure 1**. To overcome the inertness of the graphene surface on SiO_2[15,16] and increase the selectivity of the deposition in the target areas, we utilized our recently developed TPO method via fs-laser irradiation in an ambient atmosphere.[23a,29] Following the successful functionalization of selected 2x2 um^2 areas with oxygen-containing groups, we deposited 3-20 nm Eu-BDC films on the 18 graphene chips using ALD/MLD (Table S1). We used $Eu(thd)_3$ and BDC as precursor molecules and varied the number of ALD/MLD cycles and temperature to achieve the desired thickness (see experimental section in SI for details). The choice of Eu-BDC thin films was made as this is a well-studied ALD/MLD process, where the growth is well controlled.[27a,30] For graphene transfer, we used two different polymers: PMMA and PVAc. All the ALD/MLD films were amorphous, as deduced from grazing incidence X-ray diffraction measurements on Si.[30b]
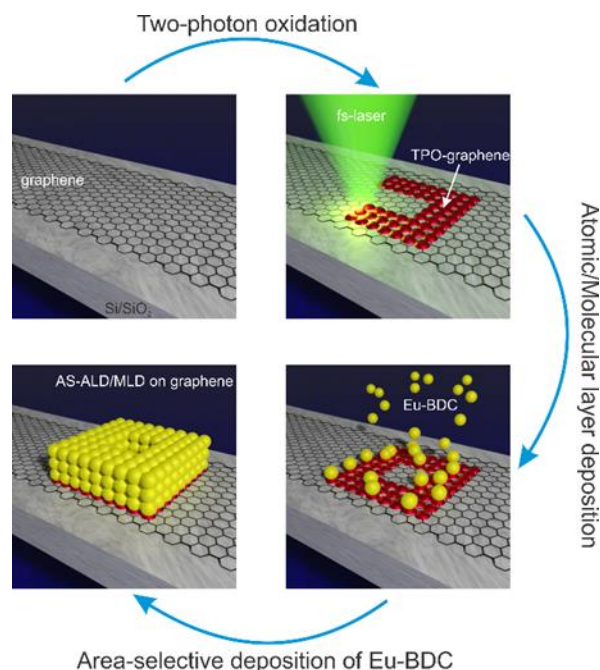
Figure 1. Scheme of the experiment, including TPO of graphene and AS-ALD/MLD deposition of Eu-BDC thin films in predefined areas.

AFM images of PVAc-transferred graphene (PVAc graphene) after TPO (**Figure 2a**) and 50 ALD/MLD cycles of Eu-BDC at 250°C (Figure 2b) show selective deposition on predefined 2x2 um^2 areas with UDLW. The thickness of the Eu-BDC films had a little variation with the laser dose and was ≈7.1 nm for 158 pJ^{2}s, while deposition on pristine graphene occurred only on wrinkles and polymer residues, with an average thickness of 0.19±0.1 nm (Figure 2c). When the deposition was performed on PMMA-transferred samples (PMMA graphene) at 250°C (Figure S1), the Eu film thickness was ≈6.6 nm at 158 pJ^{2}s, however, the average thickness on the pristine graphene surface increased to 0.71±0.3 nm. The loss of selectivity due to surface contamination by polymer residues was more pronounced for AS-ALD/MLD deposition performed at a lower temperature of 200°C (Figure S1). Differences in the chemical structures between PMMA and PVAc affected the interaction of their residues with precursors on pristine graphene areas. Although UDLW is a maskless method, polymer residues from the graphene transfer process significantly affect the selectivity of material deposition. Figures 2a and 2b show that Eu-BDC film growth on pristine graphene occurred only on residues already visible before the ALD/MLD process and on graphene wrinkles. To address this issue, employing dry transfer methods or depositing on freshly grown graphene can be effective solutions.[15,31] These residues often enhance nucleation during the ALD and MLD processes on 2DM, and selecting a precursor that interacts less strongly with commonly used polymers could be a promising area for further research.
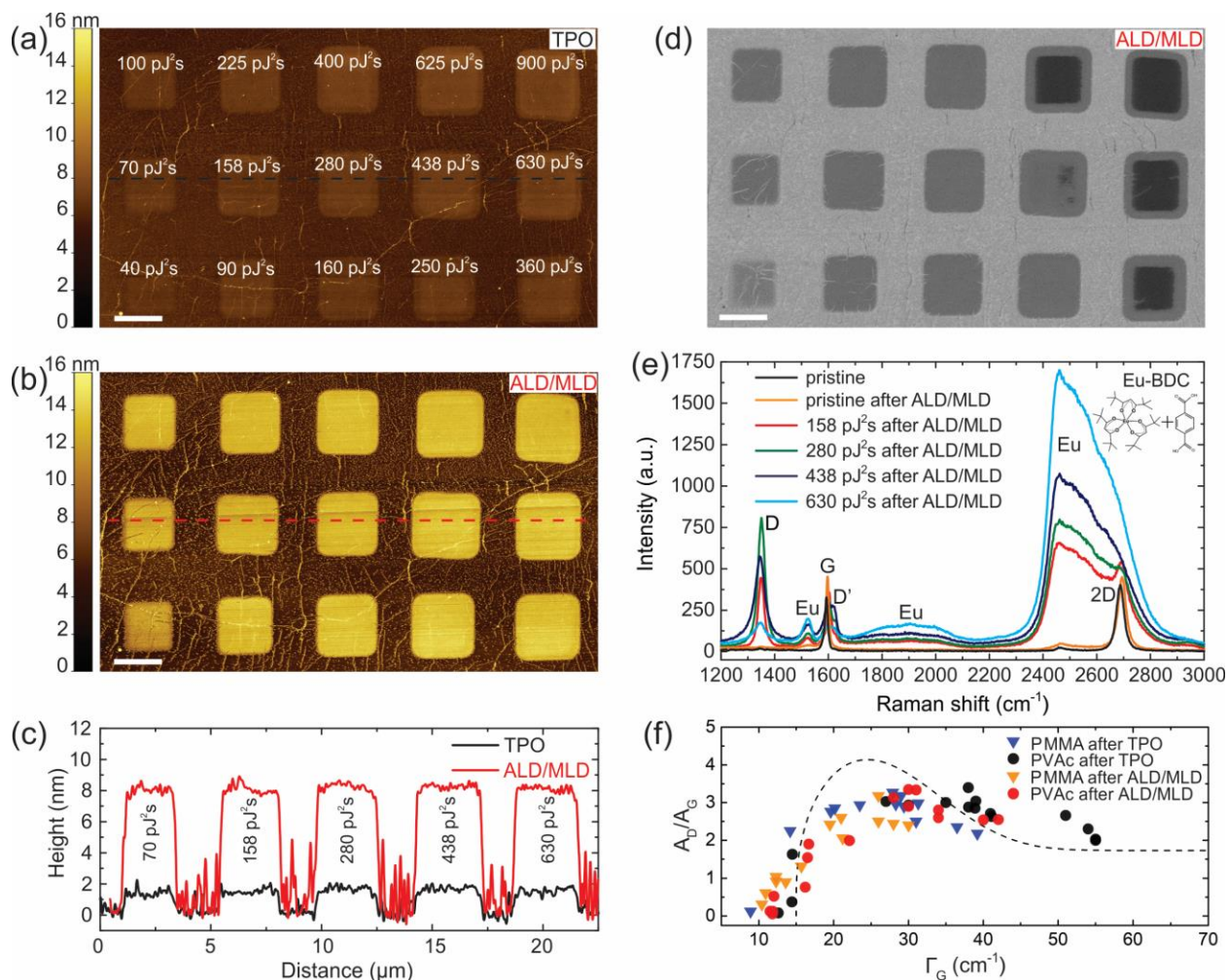
Figure 2. a) AFM image of PVAc graphene after TPO with various fs-laser irradiation doses. b) AFM image of the same sample after 50 ALD/MLD cycles of Eu-BDC. c) AFM profiles before and after ASD measured from a) and b). d) HIM image after ALD/MLD. The scale bars in a), b), and d) are 2 µm. e) Raman spectra of pristine graphene before and after 50 ALD/MLD cycles of Eu-BDC, and of four TPO areas after 50 ALD/MLD cycles of Eu-BDC. f) A_D/A_G vs. Γ_G after TPO and ALD/MLD on PVAc and PMMA graphene. The dashed line represents the simulation curve corresponding to the generated point-like defects.

Secondary electron images obtained using a helium ion microscope (HIM) after ALD/MLD of Eu-BDC show a smooth distribution of europium compound in TPO areas with sharp edges, and minimal growth in pristine graphene regions (Figure 2d). At low laser doses (<100 pJ^{2}s), the film roughness in TPO areas is affected by wrinkles. At high pulse energies exceeding 25 pJ (for doses 360 pJ^{2}s, 625 pJ^{2}s, 630 pJ^{2}s, and 900 pJ^{2}s), the graphene structure changes due to an increased amount of oxygen species, becoming porous and less conductive, as observed in the last four squares of the HIM image.

We used Raman spectroscopy to probe graphene functionalization and further investigate the selectivity of Eu-BDC AS-ALD/MLD on graphene. Figure 2e demonstrates that only a small blueshift of the G ($\approx$1590 cm^{-1}) and 2D ($\approx$2680 cm^{-1}) bands was observed after the deposition of a thin Eu-BDC film on pristine graphene. This shift is most probably caused by thermal annealing at 250°C during the ALD/MLD process. In the TPO areas, showing an increased D ($\approx$1350 cm^{-1}) band and an additional D' ($\approx$1625 cm^{-1}) band due to the oxidation process (see Figure S2),[29] three additional bands appeared after the Eu-BDC deposition (Figure S3). Two bands at $\approx$1900 cm^{-1} (corresponding to 592 nm emission wavelength) and $\approx$2450 cm^{-1} (corresponding to 612 nm) are associated with electronic transitions of the Eu-BDC film,[30b] and their intensity increases with the laser dose, which correlates with the thickness and homogeneity of the film. A third band at $\approx$1525 cm^{-1} (579 nm) also corresponds to an electronic transition in Eu-BDC. The FTIR spectrum of a 100 nm Eu-BDC film deposited on a Si substrate (see Figure S4) shows two main bands at $\approx$1394 cm^{-1} and $\approx$1545 cm^{-1}, corresponding to the asymmetric and symmetric stretching of the bonded carboxylate groups near the Eu^{3+} ion.[32] While the asymmetric stretching of the carboxylate group is close to the third band in the Raman spectrum at $\approx$1525 cm^{-1}, it is not Raman active[33] but can be activated via surface-enhanced Raman spectroscopy with the appropriate substrate.[34]

We also carried out nano-FTIR spectroscopy on pristine graphene and graphene/Eu-BDC films via infrared scattering scanning near-field optical microscopy to study the distribution of Eu-BDC on graphene at the nanoscale. While pristine graphene shows no IR bands in the region of interest, the graphene/Eu-BDC film demonstrates two distinct peaks at $\approx$1402 and $\approx$1562 cm^{-1} (Figure S5), similar to those observed for a thicker Eu-BDC film on Si. When comparing transmission FTIR and nano-FTIR spectra, the band positions may shift by a few wavenumbers. However, a more significant blueshift may indicate stronger electronic interactions between graphene and the thin Eu-BDC film compared to the film on Si.

To assess the crystallinity of graphene and its variation after TPO and ALD/MLD, we calculated the A_D/A_G ratios and defect concentration (n_D) from the measured Raman spectra (Figure S6 and Table S2). Figure 2f shows the A_D/A_G ratio as a function of the full width at half maximum (Γ_G) of the G band for PVAc and PMMA graphene before and after TPO and 50 ALD/MLD cycles of Eu-BDC. The defects generated in graphene by UDLW correspond to point-like defects.[35] After the ALD/MLD process, a decrease in the A_D/A_G ratio and a narrowing of Γ_G were observed, especially for PMMA graphene films. Thermal annealing at 250°C during the ALD/MLD partially restored the laser-induced point-like defects and improved the crystallinity of graphene. Additionally, the chemical interaction between the graphene and Eu-BDC film weakened due to the reduced number of oxygen-containing defects on the surface. Thus, even if defects are generated in graphene upon UDLW, the intrinsic properties of the layer can be restored during ALD/MLD at 250°C when small to moderate fs-laser irradiation doses are used. At higher laser pulse energies (>25 pJ), it becomes harder to control the defect density, which can result in an increase of n_D after the ALD/MLD process (Figure S6b).

What Affects the Selectivity of ALD/MLD on Graphene?

The thickness of the ALD/MLD Eu-BDC films showed little variation with the laser dose for PVAc graphene layers within 50 cycles (**Figure 3a**). However, a small variation in thickness was observed for 100 cycles and doses below 70 pJ^{2}s. Graphene transferred via PMMA demonstrated a higher dependence on the laser dose, with thickness saturation occurring only after 100 pJ^{2}s for 50 cycles and 360 pJ^{2}s for 100 cycles, respectively. This variation can be attributed to the presence of polymer residues, particularly for PMMA, which may inhibit the oxidation of graphene at low fs-laser doses and reduce the number of functional groups in the TPO area. In our further analysis, we used the heights of the ALD/MLD films measured within the laser dose range of 225-438 pJ^{2}s, where all studied samples showed saturation of film thickness (see Figure 3a).

Figure 3b shows the Eu-BDC film thickness measured on SiO$_2$ and graphene using AFM as a function of ALD/MLD cycles. The growth on the SiO$_2$ surface demonstrates a linear dependence, however, the GPC of ≈1.94±0.03 Å/cyc at 250°C is slightly lower than on the Si substrate (see experimental details in SI). We found that the Eu-BDC film grows on TPO graphene without a noticeable nucleation delay, and all the samples exhibit nearly linear growth within the first 75 cycles, with the GPC of ≈1.45±0.02 Å/cyc (PVAc at 250°C), ≈1.30±0.12 Å/cyc (PMMA at 200°C), and ≈1.47±0.17 Å/cyc (PMMA at 250°C). After 75 cycles, the GPC of the Eu-BDC film grown on TPO PMMA graphene at 200°C increases, while for films grown at 250°C, GPC saturation is observed. GPC saturation after 75 cycles is also visible for thin films grown on TPO PVAc graphene. The thicknesses of the deposited films for the same number of ALD/MLD cycles differ between TPO graphene and the SiO$_2$ substrate due to the more chemically inert surface of graphene.

The average thickness measured on pristine graphene after the ALD/MLD process at 250°C shows a nucleation delay of at least ≈50 cycles for PVAc graphene. Growth on PMMA graphene at 200°C occurred already after 25 cycles and demonstrates exponential behavior, whereas at 250°C, growth is suppressed due to weaker interaction between the precursor molecules and the pristine graphene surface.

The selectivity of the deposition can be assessed by measuring the thickness of the Eu-BDC films on TPO and pristine graphene.[9] To demonstrate the selectivity of our method, we tested four different film thicknesses, two transfer polymers, and two different temperatures. The selectivity of ALD/MLD was calculated as:

$$Selectivity = \frac{\theta_{GA} - \theta_{NGA}}{\theta_{GA} + \theta_{NGA}}$$

where θ_{GA} and θ_{NGA} are the amount of material present after ALD/MLD on the growth and non-growth areas, respectively.[36] The selectivity of the ALD/MLD process at 250°C for PVAc graphene films exceeds 0.9[37] up to 11 nm (Figure 3c), which is sufficient for fabricating a heterostructure device.[17b] While PMMA graphene samples demonstrate lower selectivity than PVAc chips for thicknesses below 12 nm, the difference vanishes as the Eu-BDC film thickness increases.
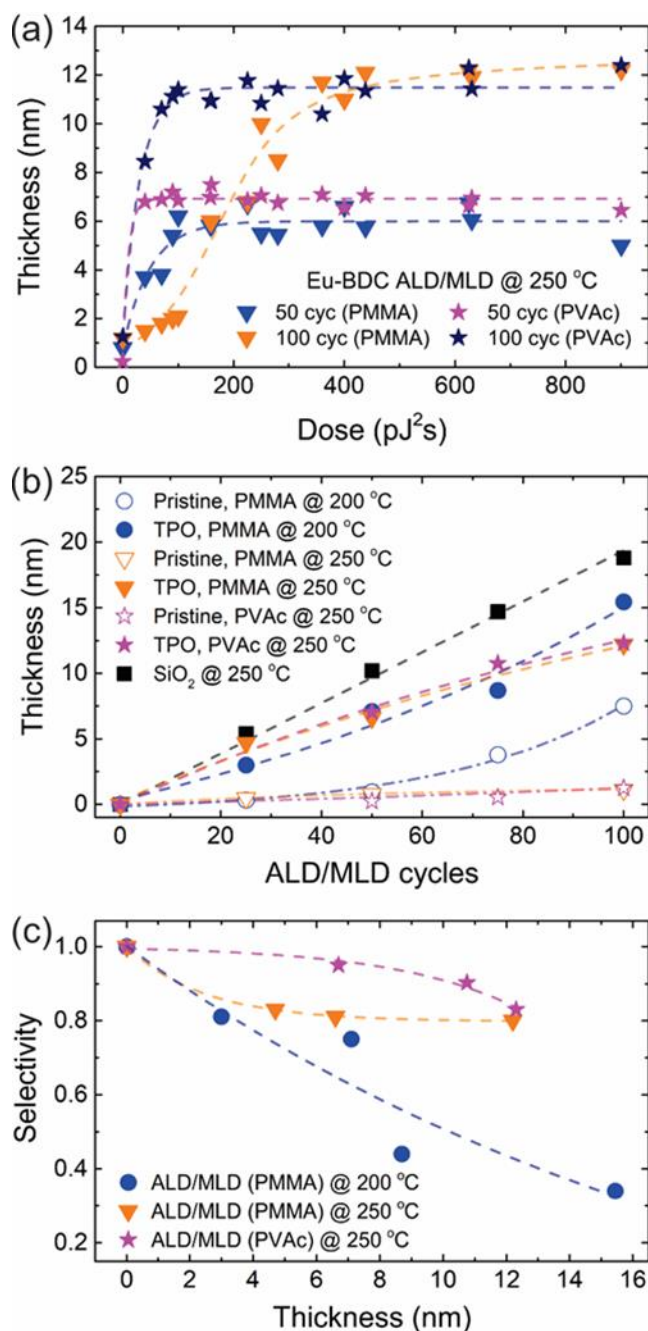
Figure 3. a) Thickness vs. fs-laser dose for PMMA and PVAc graphene samples after 50 and 100 ALD/MLD cycles of Eu-BDC at 250°C. b) Thickness vs. number of ALD/MLD cycles, measured for TPO graphene in the laser dose range of 225-438 pJ^2s and for pristine graphene areas. c) Selectivity vs. thickness, measured in the 225-438 pJ^2s dose range. Dotted lines are guides to the eye.

When the temperature decreases from 250°C to 200°C, selectivity drops due to the increased interaction of reactive precursor molecules with the pristine graphene surface. A significant

decrease in selectivity was observed, dropping from 75% at 5 nm to 35% at 15 nm. Nucleation on wrinkles and other defects also reduces the selectivity of ASD on CVD graphene, as previously demonstrated for HfO_2.[38] In addition, adsorbed impurities from the air can enhance ALD/MLD nucleation in pristine graphene areas. We did not test ALD/MLD at temperatures exceeding 300°C due to the partial decomposition of oxygen-containing groups in TPO areas[22,39] and the reduced reactivity of precursor molecules with the surface,[40] which could drastically decrease the selectivity and GPC of AS-ALD/MLD. Therefore, deposition at temperatures above 250°C on TPO graphene areas is required for AS-ALD/MLD of Eu-BDC films with selectivity exceeding 0.9. Alternatively, less reactive precursors could be used to perform the deposition at lower temperatures.

To achieve more conformal coverage on the pristine surfaces of 1D and 2DM, the physical adsorption of precursor molecules can be utilized at lower temperatures.[41] However, nonspecific physical adsorption compromises the selectivity of ALD and MLD. This challenge can be addressed by utilizing the physisorption and diffusion of ALD precursors in superlattice-based ASD, as demonstrated for MoS_2 (blocking area) and $MoSe_2$ (deposition area) crystal structures.[21] In our case, the ASD process is driven by chemisorption. Annealing during ALD/MLD restores the graphene surface at low and moderate fs-laser doses, reducing the chemical interaction with the film, as observed in the Raman spectra (see Figures 2f and S4). At moderate to high doses, the interaction between graphene and Eu-BDC films remains strong. By carefully tuning the fs-laser dose, it is possible to control the interaction strength. A weaker interaction is preferable for transistor applications, while a stronger interaction is advantageous in designing graphene-based heterostructures that require enhanced electron transfer between graphene and functional films, for example, in optoelectronics and photonics.

We also studied how the pre-annealing step affects the selectivity of ALD/MLD deposition on graphene. Annealing in an Ar/H_2 atmosphere reduced the amount of PMMA residues and enhanced the selectivity for Eu-BDC deposition (see Figures 3, S7, and Table S1). Annealing in an O_2 atmosphere increased the number of defects in the pristine graphene layer and promoted the growth of the Eu-organic film outside the TPO areas. For PVAc graphene, the result was the opposite. While ALD/MLD on the unannealed graphene surface resulted in a nucleation delay of at least ≈50 cycles, for annealed PVAc graphene samples in an Ar/H_2 atmosphere, the selectivity dropped to 0.7 already after 25 cycles. This may be due to the decomposition of PVAc and the presence of amorphous carbon after annealing at 350°C in an inert atmosphere. Thus, we argue that the interaction of precursor molecules with PVAc is much weaker compared to PMMA and amorphous carbon.

Graphene/Eu-Organic Heterostructures

Figures 4a and 4b show the AFM and surface potential images of the graphene/Eu-BDC structures after ASD of a ≈7.1 nm Eu-BDC film. The three distinct squares correspond to TPO graphene regions irradiated with fs-laser doses of 40, 90, and 160 pJ^2s. The height and work function (WF) profiles are shown in Figure 4c. The surface potential image was obtained using

Kelvin probe force microscopy (KPFM) with an Au-coated AFM tip, and the WF values were calculated by subtracting the surface potential from the known work function of Au (5.3 eV).

The WF of pristine graphene was measured at 4.75±0.05 eV, while the TPO graphene areas exhibited higher WF values of 5.06 eV at 90 pJ^{2}s and up to 5.27 eV for 625 pJ^{2}s (Figure S8), indicating significant p-type doping due to the binding of oxygen-containing groups to the graphene surface. The deposition of 50 ALD/MLD cycles of Eu-BDC at 250°C slightly reduced the WF by ≈35 meV in the 90 pJ^{2}s area. For 160 pJ^{2}s, it decreased further by ≈100 meV, reaching 4.96 eV. This reduction in WF after Eu-BDC deposition suggests n-type doping at higher fs-laser doses, driven by increased charge transfer between the Eu-BDC film and graphene.
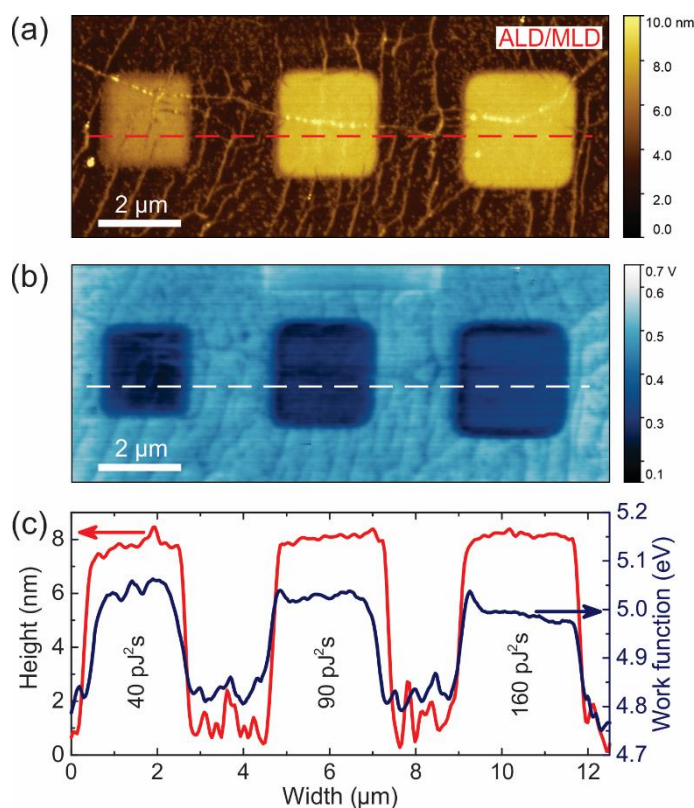

Figure 4. a) AFM image of PVAc graphene after 50 ALD/MLD cycles of Eu-BDC. b) Surface potential distribution of PVAc graphene after 50 ALD/MLD cycles of Eu-BDC measured via KPFM. c) Height and work function profiles measured from dashed lines in a) and b).

After the ALD/MLD process, the G and 2D bands in the Raman spectrum of pristine graphene show a blueshift, indicating p-type doping due to the enhanced interaction between graphene and the underlying SiO$_2$ substrate, increased by annealing at 250°C during deposition in an inert atmosphere. In the TPO areas, the blueshift of the G and 2D bands diminishes as the fs-laser

dose increases (Figures S3 and S9). At 160 pJ^{2}s, the 2D band shows a 2 cm^{-1} redshift, demonstrating that the charge transfer mechanism is more pronounced at higher fs-laser doses.

A comparison of the KPFM and Raman results shows that higher laser doses promote stronger interactions between the Eu-BDC film and graphene, leading to a decreased WF and a shift toward n-type doping. The ability to fine-tune the electronic properties of graphene/Eu-BDC heterostructures by controlling the fs-laser dose, ASD, and annealing conditions opens novel perspectives in 2DM electronic, optoelectronic, and sensor applications, where precise work function modulation is essential for optimizing device performance. Variations in ALD/MLD film thickness can also affect the built-in electric field generation in p-n junctions upon incident light illumination.[42]

Luminescent Properties of Graphene/Eu-Organic Heterostructures

To investigate the potential applications of graphene/Eu-organic heterostructures in photonics and imaging, we studied the Photoluminescence (PL) signal, and its lifetime, as well as the effects of the laser irradiation dose on these properties. Micro-PL spectra collected from different areas of the sample after 100 ALD/MLD cycles of Eu-BDC upon 532 nm laser excitation (**Figure 5a**) revealed four characteristic PL peaks of Eu^{3+} located at ≈579 nm, ≈592 nm, ≈612 nm (the most intense and sharp red emission line), and ≈652 nm for Eu-BDC on SiO$_2$ and TPO graphene. For pristine graphene with minimal Eu-BDC deposition, only the peaks at ≈579 nm and ≈612 nm were visible due to the small amount of PL material.

We attribute the excitation at 532 nm to a pure magnetic dipole transition $^7F_0 \rightarrow {}^5D_1$, which peaks at 526 nm (Figure 5b).[43,44] The $^5D_1$ state then relaxes non-radiatively to the level $^5D_0$, which emits via the $^5D_0 \rightarrow {}^7F_j$ (j = 0, 1, 2, 3) transitions. However, the emission may also occur via $^5D_1 \rightarrow {}^7F_j$ transitions with a much shorter lifetime.[43]

A strong PL signal after ALD/MLD centered at ≈612 nm was detected on TPO graphene prepared with a relatively low irradiation dose of 90 pJ^{2}s, and the signal intensity increased with higher TPO irradiation doses (Figure 5c). The PL intensity from the TPO areas was up to 20 times higher at a fs-laser dose of 158 pJ^{2}s and up to 52 times higher at 625 pJ^{2}s dose compared to the PL signal from pristine graphene areas after 50 ALD/MLD cycles (Figure 2e). However, after 100 ALD/MLD cycles, the enhancement of PL intensity in the TPO areas decreased, and was ≈15 and ≈20 times stronger, respectively, due to the partial deposition of Eu-BDC on the pristine graphene areas (Figure 5a). Overall, this provides strong evidence of precise AS-ALD/MLD deposition of Eu-BDC films on TPO graphene and demonstrates the ability to localize luminescence using selective deposition.

In a few samples, we also detected a peak at ≈566 nm upon CW laser illumination (Figure S10). These emissions indicate contributions from $^5D_1 \rightarrow {}^7F_2$ (≈566 nm) and $^5D_1 \rightarrow {}^7F_3$ (≈579 nm) transitions to the PL spectrum of the ALD/MLD films when direct excitation of the $^5D_1$ level occurs.[43,45] Interestingly, the green emission at ≈566 nm was observed only on pristine and TPO

graphene and was absent on Si and SiO_2. Note that 532 nm excites the $^5D_1$ level and we do not consider transitions from higher energy states.
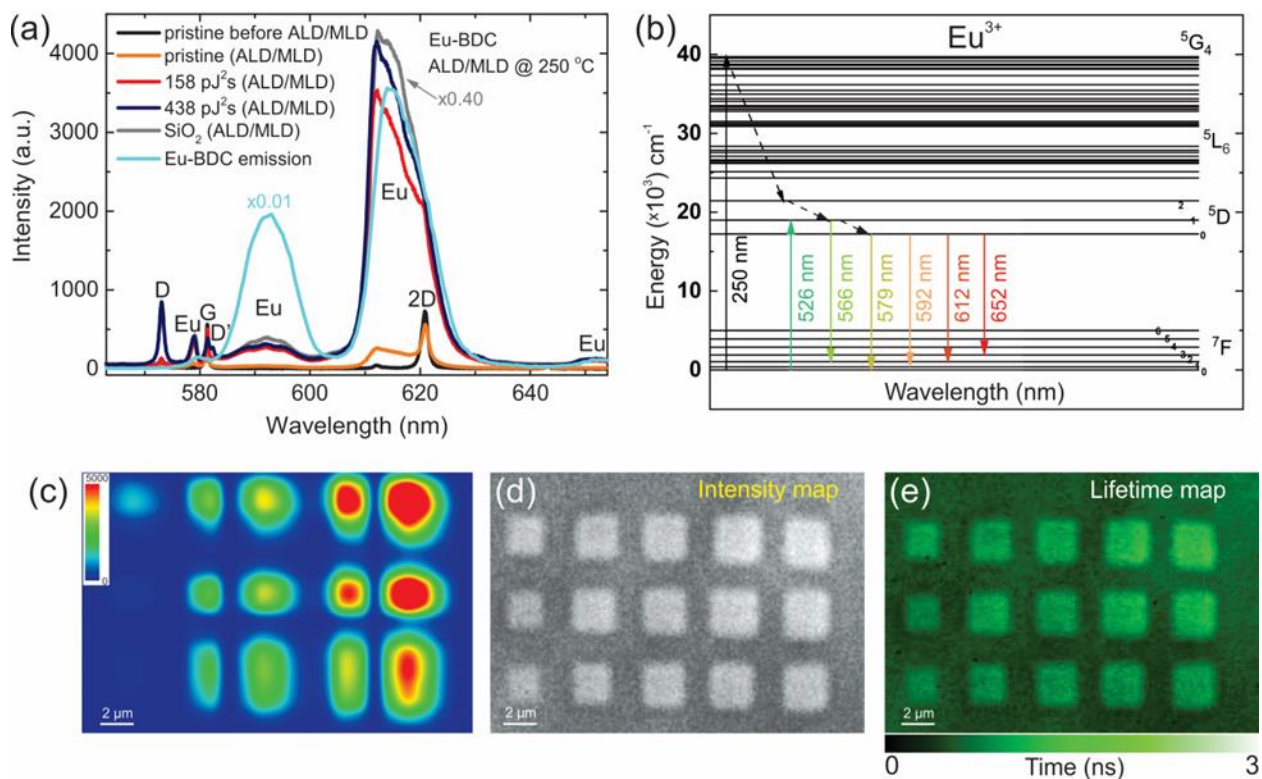

Figure 5. a) Micro-PL spectra of Eu-BDC films after 100 ALD/MLD cycles on SiO_2, pristine graphene, and TPO graphene (158 and 438 pJ^2s) excited by a 532 nm CW laser, along with the emission spectrum of a 100 nm Eu-BDC film on Si excited by a 150 W Xe arc lamp at 250 nm. b) Energy-level scheme of the Eu^{3+} ion. c) Micro-PL map of the Eu-BDC film after 100 ALD/MLD cycles, measured at 612 nm and excited by a 532 nm CW laser. d) FLIM intensity map of the Eu-BDC film after 50 ALD/MLD cycles, excited by 514 nm ps-laser. (e) FLIM lifetime map of the Eu-BDC film after 50 ALD/MLD cycles, excited by a 514 nm ps-laser.

When excited by a 532 nm CW laser, the intensities of the PL peaks at ≈566 nm and ≈579 nm, relative to the peak at ≈612 nm, are significantly higher for Eu-BDC on graphene compared to the 100 nm Eu-BDC film on Si, which was excited at 250 nm (Figures 5a and S11). Therefore, the emission from the $^5D_1$ level is enhanced compared to the emission from the $^5D_0$ level for Eu-BDC films on pristine and TPO graphene. The $^7F_0 \rightarrow {}^5D_1$ pure magnetic dipole transition, excited by a 532 nm laser, populates the $^5D_1$ level. One possible enhancement mechanism could be the suppression of non-radiative relaxation to the $^5D_0$ level, but it is difficult to identify any graphene-induced process responsible for this. Another possibility is an enhanced radiative rate from the $^5D_1$ state to ^7F_j, however, we are not aware of any graphene-induced mechanism behind this. A third possibility is a thermally activated enhancement of the $^5D_1$ state population, potentially caused by laser-induced heating of graphene. We tested this hypothesis by measuring the PL spectra at different excitation powers (Figure S12a), but the results did not show enhanced emission with increased power. Additionally, the PL intensity of the peak at ≈612 nm

after 532 nm CW laser excitation demonstrates a linear response (Figure S12b), showing that no two-photon absorption processes are involved in signal generation. Thus, the mechanism behind this enhancement remains unclear.

We also observed quenching of the PL signal on the TPO graphene surface compared to SiO_2 (Figure 5a). This is primarily attributed to Förster resonance energy transfer, enabled by the linear dispersion of Dirac electrons,[46] which indicates a significant energy transfer between the Eu-BDC film and graphene. Alternatively, the quenching effect could be due to electron transfer. After excitation of the Eu^{3+}, an excited electron can transfer to the graphene conduction band, leading to fluorescence quenching.[47]

Fluorescence quenching also affects the lifetime of Eu-BDC on graphene. We performed fluorescence lifetime imaging microscopy (FLIM) measurements to investigate the fluorescence dynamics of ALD/MLD Eu-BDC thin films on pristine and TPO graphene. While the overall fluorescence intensity (Figure 5d) was low upon 514 nm pulsed laser excitation, the lifetime of Eu-BDC on TPO areas was significantly longer than on pristine graphene (Figure 5e). The measured lifetime of ~2-3 ns is much shorter than the reported lifetimes for Eu^{3+} films (~10 µs for transitions originating from the $^5D_1$ state[43] and ~1.5 ms for transitions from the $^5D_0$ state). Lifetimes in the ns range could be explained by fluorescence quenching due to energy and charge transfer between graphene and Eu-BDC. We demonstrated that the fluorescence dynamics of uncoated graphene was not affected by the TPO process itself by performing FLIM measurements after UDLW (Figure S13a,b). No visible signal was detected when the surface was irradiated with the same fs-laser doses and measured under the same conditions as in Figure 5e. However, other mechanisms, in addition to energy and electron transfer to graphene, might be involved, as short lifetimes were also observed for Eu-BDC thin films on SiO_2 (Figure S13c,d). Notably, Eu-BDC demonstrates very weak absorption at the laser wavelengths used (514 and 532 nm).[30b] Therefore, the PL is expected to be much stronger upon resonant excitation in the UV range. The observed properties of Eu-BDC/graphene heterostructures could have potential applications in bioimaging, where tunable photoluminescence may enable precise tracking of biological processes in real time,[48] and in solar cells, where enhanced electron transfer could improve charge separation efficiency.[1b]

Conclusion

In summary, we successfully demonstrated the area-selective ALD/MLD of Eu-organic thin films on single-layer graphene using fs-laser TPO to locally activate predefined regions. We achieved high homogeneity and over 90% selectivity for Eu-organic films up to 11 nm, overcoming the chemical inertness of graphene. The choice of polymer for graphene transfer significantly affected selectivity, as it might leave residues and promote undesired deposition on pristine graphene. The fabricated graphene/Eu-organic heterostructures exhibited strong PL emission upon 532 nm excitation, while Eu^{3+} ions typically require UV excitation. Efficient electron and energy transfer via fluorescence quenching were demonstrated through work function, Raman, and fluorescence lifetime measurements at fs-laser doses above 160 pJ^{2}s.

The AS-ALD/MLD method can be extended to various metal-organic thin films with tailored properties, such as magnetic or thermoelectric materials, allowing for the design of novel heterostructures for electronic, optoelectronic, and photonic applications. Sub-micrometer precision was demonstrated on graphene, significantly expanding the possibilities for multifunctional devices on a single chip. Further optimization of the ALD/MLD and UDLW processes could enable better control of thin film growth at the sub-20 nm scale, comparable to current CMOS technology.

Supporting Information

The authors have cited additional references within the Supporting Information.[22,25,30b,40,49]

Acknowledgements

References

[1]   a) M. Gobbi, E. Orgiu, P. Samorì, *Adv. Mater.* **2018**, *30*, 1706103; b) Y. Zhao, L. Zhang, J. Liu, K. Adair, F. Zhao, Y. Sun, T. Wu, X. Bi, K. Amine, J. Lu, X. Sun, *Chem. Soc. Rev.* **2021**, *50*, 3889–3956; c) Y. Zhao, X. Sun, *ACS Energy Lett.* **2018**, *3*, 899; d) J. Wu, M. Gong, *J. Appl. Phys.* **2021**, *130*, 70905; e) X. Chen, K. Shehzad, L. Gao, M. Long, H. Guo, S. Qin, X. Wang, F. Wang, Y. Shi, W. Hu, Y. Xu, X. Wang, *Adv. Mater.* **2020**, *32*, 1902039; f) H. L. Hou, C. Anichini, P. Samorì, A. Criado, M. Prato, *Adv. Funct. Mater.* **2022**, *32*, 2207065; g) L. Wang, B. Li, Z. You, A. Wang, X. Chen, G. Song, L. Yang, D. Chen, X. Yu, J. Liu, C. Chen, *Anal. Chem.* **2021**, *93*, 11123.

[2]   a) L. Jia, J. Wu, Y. Zhang, Y. Qu, B. Jia, Z. Chen, D. J. Moss, *Small Methods* **2022**, *6*, 2101435; b) K. Zhu, C. Wen, A. A. Aljarb, F. Xue, X. Xu, V. Tung, X. Zhang, H. N. Alshareef, M. Lanza, *Nat. Electron.* **2021**, *4*, 775.

[3]   a) S. M. George, *Chem. Rev.* **2010**, *110*, 111; b) J. Multia, M. Karppinen, *Adv. Mater. Interfaces* **2022**, *9*, 2200210; c) S. Yasmeen, S. W. Ryu, S.-H. Lee, H.-B.-R. Lee, *Adv. Mater. Technol.* **2023**, *8*, 2200876.

[4]   T. Yoshimura, S. Tatsuura, W. Sotoyama, *Appl. Phys. Lett.* **1991**, *59*, 482.

[5]   a) A. Philip, J. P. Niemelä, G. C. Tewari, B. Putz, T. E. J. Edwards, M. Itoh, I. Utke, M. Karppinen, *ACS Appl. Mater. Interfaces* **2020**, *12*, 21912; b) G. Wang, Y. Duan, *SmartMat* **2024**, e1286.

[6]   G. N. Parsons, R. D. Clark, *Chem. Mater.* **2020**, *32*, 4920.

[7]   G. H. Baek, H. L. Yang, G. B. Park, J. S. Park, *Jpn. J. Appl. Phys.* **2023**, *62*, SG0810.

[8]   W. H. Kim, F. S. Minaye Hashemi, A. J. M. Mackus, J. Singh, Y. Kim, D. Bobb-Semple, Y. Fan, T. Kaufman-Osborn, L. Godet, S. F. Bent, *ACS Nano* **2016**, *10*, 4451.

[9]   A. J. M. Mackus, M. J. M. Merkx, W. M. M. Kessels, *Chem. Mater.* **2019**, *31*, 2.

[10]   A. K. Mandal, M. H. van der Veen, N. R. Haghighi, M. Robson, N. Claessens, J. Meersschaut, N. Jourdan, Z. Tokei, A. Delabie, M. Robson, *Adv. Mater. Technol.* **2024**, *9*, 2301820.

[11]   a) C. Prasittichai, H. Zhou, S. F. Bent, *ACS Appl. Mater. Interfaces* **2013**, *5*, 13391; b) J. J. Brown, R. A. Hall, P. E. Kladitis, S. M. George, V. M. Bright, *ACS Nano* **2013**, *7*, 7812; c) R. A. Nye, V. Dongen, J.-F. De Marneffe, G. N. Parsons, A. Delabie, *Adv. Mater. Interfaces* **2023**, *10*, 2300163; d) H. Oh, J. M. Thelven, H. R. M. Margavio, G. N. Parsons, *Adv. Funct. Mater.* **2024**, 2316872.

[12]   a) L. K. Tan, B. Liu, J. H. Teng, S. Guo, H. Y. Low, K. P. Loh, *Nanoscale* **2014**, *6*, 10584; b) S. Balasubramanyam, M. J. M. Merkx, M. A. Verheijen, W. M. M. Kessels, A. J. M. Mackus, A. A. Bol, *ACS Mater. Lett.* **2020**, *2*, 511.

[13]   a) J. Yarbrough, A. B. Shearer, S. F. Bent, *J. Vac. Sci. Technol. A* **2021**, *39*, 21002; b) C. T. Nguyen, E. H. Cho, B. Gu, S. Lee, H. S. Kim, J. Park, N. K. Yu, S. Shin, B. Shong, J. Y. Lee, H. B. R. Lee, *Nat. Commun.* **2022**, *13*, 7597; c) C. T. Nguyen, E. H. Cho, N. Le Trinh, B. Gu, M. Lee, S. Lee, J. Y. Lee, Y. Kang, H. B. R. Lee, *Chem. Mater.* **2023**, *35*, 5331.

[14]   A. J. M. Mackus, A. A. Bol, W. M. M. Kessels, *Nanoscale* **2014**, *6*, 10941.

[15]   a) B. Dlubak, P. R. Kidambi, R. S. Weatherup, S. Hofmann, J. Robertson, *Appl. Phys. Lett.* **2012**, *100*, 173113; b) K. Kim, H. B. R. Lee, R. W. Johnson, J. T. Tanskanen, N. Liu, M. G. Kim, C. Pang, C. Ahn, S. F. Bent, Z. Bao, *Nat. Commun.* **2014**, *5*, 4781.

[16]   R. H. J. Vervuurt, W. M. M. E. Kessels, A. A. Bol, *Adv. Mater. Interfaces* **2017**, *4*, 1700232.

[17]   a) J. M. P. Alaboson, Q. H. Wang, J. D. Emery, A. L. Lipson, M. J. Bedzyk, J. W. Elam, M. J. Pellin, M. C. Hersam, *ACS Nano* **2011**, *5*, 5223; b) X. Liu, B. Yang, X. Zhou, M. Wu, E. Spiecker, J. Bachmann, F. Hauke, A. Hirsch, T. Wei, *Angew. Chem. Int. Ed.* **2023**, *62*, e202314183.

[18]   a) M. Xiao, C. Qiu, Z. Zhang, L. M. Peng, *ACS Appl. Mater. Interfaces* **2017**, *9*, 34050; b) G. Koerner, Q. K. Wyatt, B. Bateman, C. Boyle, M. J. Young, M. R. Maschmann, C. R. M. Maschmann, *Nano Select* **2022**, *3*, 1448.

[19]   G. Park, D. Go, S. Jo, T. H. Lee, J. W. Shin, J. An, *Adv. Electron. Mater.* **2023**, *9*, 2300074.

[20]   a) O. M. Nayfeh, T. Marr, M. Dubey, *IEEE Electron Device Lett.* **2011**, *32*, 473; b) M. Snure, S. R. Vangala, T. Prusnick, G. Grzybowski, A. Crespo, K. D. Leedy, *Sci. Rep.* **2020**, *10*, 14699; c) B. Canto, M. Otto, M. J. Powell, V. Babenko, A. O'Mahony, H. C. M. Knoops, R. S. Sundaram, S. Hofmann, M. C. Lemme, D. Neumaier, *Adv. Mater. Technol.* **2021**, *6*, 2100489.

[21]   J. Park, S. J. Kwak, S. Kang, S. Oh, B. Shin, G. Noh, T. S. Kim, C. Kim, H. Park, S. H. Oh, W. Kang, N. Hur, H. J. Chai, M. Kang, S. Kwon, J. Lee, Y. Lee, E. Moon, C. Shi, J. Lou, W.

B. Lee, J. Y. Kwak, H. Yang, T. M. Chung, T. Eom, J. Suh, Y. Han, H. Y. Jeong, Y. J. Kim, K. Kang, *Nat. Commun.* **2024**, *15*, 2138.

[22]   K. K. Mentel, A. V. Emelianov, A. Philip, A. Johansson, M. Karppinen, M. Pettersson, *Adv. Mater. Interfaces* **2022**, *9*, 2201110.

[23]   a) J. Aumanen, A. Johansson, J. Koivistoinen, P. Myllyperkiö, M. Pettersson, *Nanoscale* **2015**, *7*, 2851; b) I. I. Bobrinetskiy, A. V. Emelianov, N. Otero, P. M. Romero, *Appl. Phys. Lett.* **2015**, *107*, 043104.

[24]   a) A. Johansson, H. C. Tsai, J. Aumanen, J. Koivistoinen, P. Myllyperkiö, Y. Z. Hung, M. C. Chuang, C. H. Chen, W. Y. Woon, M. Pettersson, *Carbon* **2017**, *115*, 77; b) I. Bobrinetskiy, A. Emelianov, A. Nasibulin, I. Komarov, N. Otero, P. M. Romero, *J. Phys. D: Appl. Phys.* **2016**, *49*, 41LT01.

[25]   a) F. Huth, A. Govyadinov, S. Amarie, W. Nuansing, F. Keilmann, R. Hillenbrand, *Nano Lett.* **2012**, *12*, 3973; b) J. Schirmer, R. Chevigny, A. Emelianov, E. Hulkko, A. Johansson, P. Myllyperkiö, E. D. Sitsanidis, M. Nissinen, M. Pettersson, *Phys. Chem. Chem. Phys.* **2023**, *25*, 8725.

[26]   A. V. Emelianov, M. Pettersson, I. I. Bobrinetskiy, *Adv. Mater.* **2024**, *36*, 2402907.

[27]   a) A. Ghazy, M. Lastusaari, M. Karppinen, *Chem. Mater.* **2023**, *35*, 5988; b) A. Ghazy, M. Lastusaari, M. Karppinen, *J. Mater. Chem. C* **2023**, *11*, 5331; c) A. Ghazy, J. Ylönen, N. Subramaniyam, M. Karppinen, *Nanoscale* **2023**, *15*, 15865; d) A. Ghazy, D. Zanders, A. Devi, M. Karppinen, *Adv. Mater. Interfaces* **2024**, 2400274.

[28]   a) S. Lee, M. Kim, G. Baek, H. M. Kim, T. T. N. Van, D. Gwak, K. Heo, B. Shong, J. S. Park, *ACS Appl. Mater. Interfaces* **2020**, *12*, 43212; b) S. Lee, H. M. Kim, G. H. Baek, J. S. Park, *ACS Appl. Mater. Interfaces* **2021**, *13*, 60144.

[29]   A. V. Emelianov, D. Kireev, A. Offenhäusser, N. Otero, P. M. Romero, I. I. Bobrinetskiy, *ACS Photonics* **2018**, *5*, 3107.

[30]   a) Z. Giedraityte, P. Sundberg, M. Karppinen, *J. Mater. Chem. C* **2015**, *3*, 12316; b) M. Safdar, A. Ghazy, M. Tuomisto, M. Lastusaari, M. Karppinen, *J. Mater. Sci.* **2021**, *56*, 12634.

[31]   N. Hong, D. Kireev, Q. Zhao, D. Chen, D. Akinwande, W. Li, *Adv. Mater.* **2022**, 34, 2106615.

[32]   L. Ortega-Arroyo, E. S. Martin-Martinez, M. A. Aguilar-Mendez, A. Cruz-Orea, I. Hernandez-Pérez, C. Glorieux, *Starch/Stärke* **2013**, *65*, 814.

[33]   K. Ito, H. J. Bernstein, *Can. J. Chem.* **1956**, *34*, 170.

[34]   O. Sambalova, K. Thorwarth, N. V. Heeb, D. Bleiner, Y. Zhang, A. Borgschulte, A. Kroll, *ACS Omega* **2017**, *3*, 724.

[35]   L. G. Cançado, M. G. Da Silva, E. H. Martins Ferreira, F. Hof, K. Kampioti, K. Huang, A. Pénicaud, C. A. Achete, R. B. Capaz, A. Jorio, *2D Mater.* **2017**, *4*, 025039.

[36]   W. L. Gladfelter, *Chem. Mater.* **1993**, *5*, 1372.

[37]   D. Bobb-Semple, K. L. Nardi, N. Draeger, D. M. Hausmann, S. F. Bent, *Chem. Mater.* **2019**, *31*, 1635.

[38]   I. K. Oh, J. Tanskanen, H. Jung, K. Kim, M. J. Lee, Z. Lee, S. K. Lee, J. H. Ahn, C. W. Lee, K. Kim, H. Kim, H. B. R. Lee, *Chem. Mater.* **2015**, *27*, 5868.

[39]   H. Xu, W. He, Z. Li, J. Chi, J. Jiang, K. Huang, S. Li, G. Sun, H. Dou, X. Zhang, *Adv. Funct. Mater.* **2022**, *32*, 2111131.

[40]   J. Penttinen, M. Nisula, M. Karppinen, *Chem. Eur. J.* **2017**, *23*, 18225.

[41]   a) J. S. Ko, Z. Zhang, S. Lee, M. Jaikissoon, R. K. A. Bennett, K. Kim, A. C. Kummel, P. Bandaru, E. Pop, K. C. Saraswat, *In IEEE 53rd European Solid-State Device Research Conference (ESSDERC)* **2023**, 1; b) S. Ding, Y. Liu, Q. Shang, B. Gao, F. Yao, B. Wang, X. Ma, Z. Zhang, C. Jin, *Nano Lett.* **2024**, DOI 10.1021/ACS.NANOLETT.4C03407.

[42]   S. Lin, Y. Lu, J. Xu, S. Feng, J. Li, *Nano Energy* **2017**, *40*, 122.

[43]   M. D. Chambers, P. A. Rousseve, D. R. Clarke, *J. Lumin.* **2009**, *129*, 263.

[44]   A. Ćirić, Ł. Marciniak, M. D. Dramićanin, *Sci. Rep.* **2022**, *12*, 563.

[45]   K. Binnemans, *Coord. Chem. Rev.* **2015**, *295*, 1.

[46]   L. Gaudreau, K. J. Tielrooij, G. E. D. K. Prawiroatmodjo, J. Osmond, F. J. G. De Abajo, F. H. L. Koppens, *Nano Lett.* **2013**, *13*, 2030.

[47]   W. Lin, B. Tian, P. Zhuang, J. Yin, C. Zhang, Q. Li, T. M. Shih, W. Cai, *Nano Lett.* **2016**, *16*, 5737.

[48]   X. Song, S. Li, H. Guo, W. You, X. Shang, R. Li, D. Tu, W. Zheng, Z. Chen, H. Yang, X. Chen, *Angew. Chem. Int. Ed.* **2019**, *58*, 18981.

[49]   a) K. J. Eisentraut, R. E. Sievers, *J. Am. Chem. Soc.* **1965**, *87*, 5254; b) M. M. Lucchese, F. Stavale, E. H. M. Ferreira, C. Vilani, M. V. O. Moutinho, R. B. Capaz, C. A. Achete, A. Jorio, *Carbon* **2010**, *48*, 1592.